frontiers | Frontiers in Environmental Science

TYPE Original Research
PUBLISHED 20 October 2022
DOI 10.3389/fenvs.2022.973192

OPEN ACCESS

EDITED BY
Shuisen Chen,
Guangzhou Institute of Geography, China

REVIEWED BY
Thomas Allen,
Old Dominion University, United States
Andreas Schmitt,
Munich University of Applied Sciences, Germany

*CORRESPONDENCE
Ce Zhang,
c.zhang9@lancaster.ac.uk

SPECIALTY SECTION
This article was submitted to Environmental Informatics and Remote Sensing, a section of the journal Frontiers in Environmental Science

RECEIVED 19 June 2022
ACCEPTED 10 October 2022
PUBLISHED 20 October 2022

CITATION
Wang Z, Zhang C and Atkinson PM (2022), Combining SAR images with land cover products for rapid urban flood mapping.
Front. Environ. Sci. 10:973192.
doi: 10.3389/fenvs.2022.973192

Combining SAR images with land cover products for rapid urban flood mapping

Ziming Wang[1], Ce Zhang[1,2]* and Peter M. Atkinson[1,3,4]

[1]Lancaster Environment Centre, Lancaster University, Lancaster, United Kingdom, [2]UK Centre for Ecology and Hydrology, Lancaster, United Kingdom, [3]Geography and Environmental Science, University of Southampton, Southampton, United Kingdom, [4]Institute of Geographic Sciences and Natural Resources Research, Chinese Academy of Sciences, Beijing, China

Synthetic Aperture Radar (SAR) is an indispensable source of data for mapping and monitoring flood hazards, thanks to its ability to image the Earth's surface in all weather conditions and at all times. Through cloud computing platforms such as Google Earth Engine (GEE), SAR imagery can be used in near-real time for rapid flood mapping. This has facilitated the disaster response community to make informed decisions in flood hazard interventions and management plans. However, rapid urban flood mapping using SAR is challenging, due to the complex land cover configuration in urban environments, coupled with complicated backscattering mechanisms. Here, we propose a novel method to utilise SAR imagery and land use-land cover (LULC) products for rapid urban flood mapping. Our approach uses a Land Cover Product to segment the study area into LULC types and differentiate each type with respect to whether double bounce is expected to occur during the flooding events. The normalised difference index was derived using a multi-temporal SAR image stack, and the threshold segmentation method was adopted for flood mapping. In addition, DEM and Surface Water datasets were employed to refine the flood extraction results using a morphological correction approach. We assessed the method quantitatively using two use cases: the 2017 Houston and 2022 Coraki flood events. Based on fine spatial resolution optical imagery, the proposed method achieved an accuracy of 92.7% for the August 2017 Houston flood mapping task and 89% for the March 2022 Coraki flood mapping task, which not only represents at least 13% in accuracy compared to non-LCP based flood extraction method, but also provides strong capability for rapid flood mapping in urban settings.

KEYWORDS

urban flood mapping, earth observation, synthetic aperture radar, land cover product, google earth engine

1 Introduction

Urban flooding is a major natural hazard triggered by short-term heavy rainstorms or continuous precipitation exceeding the drainage capacity (Shahapure et al., 2010; Zhang et al., 2020). In part due to a globally changing climate and excessive urbanisation, urban flooding has become increasingly frequent and resulted in severe devastation to economies (Huang et al., 2018; Fan & Matsumoto, 2020; Pervin et al., 2020; Tayyab et al., 2021). In South Korea, the economic losses in Busan metropolitan city due to urban flooding amounted to US$1.5 billion from 2007 to 2016 (Dao et al., 2020). In India, the Mumbai flooding in July 2019 killed at least 18 people and triggered massive traffic disruptions (Ke et al., 2020). In China, the flooding disaster in Zhengzhou on 20 July 2021 killed 302 people and left 50 missing (Wang et al., 2022).

Satellite Earth observation has been one of the most powerful and economically viable tools to provide valuable first-hand information in flood-affected areas. Amongst all satellite sensors and platforms, synthetic aperture radar (SAR) systems offer the benefit of sensing through clouds, allowing observation in all weather conditions and at all times. Previous studies showed that SAR systems are suitable for flood mapping, and can be used to generate near real-time flood maps relevant to urban flood management (Pulvirenti et al., 2016; Cohen et al., 2019).

The major task of urban flood mapping using SAR is to distinguish between flooded and non-flooded areas using the pixel values. Currently used methods include threshold segmentation and supervised classification (Zhou et al., 2019). Threshold segmentation is performed by a backscatter diagram to identify the most appropriate threshold for segmentation. Supervised classification uses a supervised learning algorithm with a set of training data selected from the SAR images to train the model for classification (Li and Niu, 2020; Peng et al., 2021).

Supervised classification methods such as Random Forest, Bayesian Model or the state-of-the-art Deep Learning often require large numbers of training samples to achieve sufficient classification accuracy. However, flooded areas are often associated with thick cloud cover, and it is challenging to acquire high quality training samples. On the contrary, threshold segmentation methods do not require a massive dataset to train the model and are based purely on statistical distribution information from the data. Nevertheless, optimal threshold selection is difficult, with different flood cases showing a diverse range of backscatter. Moreover, mapping floods based on a single threshold only cannot represent real-world scenarios, particularly in complicated urban environments (Li and Niu, 2020). In terms of data source, instead of working directly on SAR images, these two methods can also operate on normalised difference index (NDI) images for flood mapping. The NDI values of pixels before and after flooding are derived using multi-temporal SAR imagery based on Change Detection (CD) approaches (Long et al., 2014; Pulvirenti et al., 2016).

Despite the above, urban flood mapping remains an extremely challenging task, due to the complexity of urban surface types and the complicated backscattering mechanisms, whether original SAR or NDI images are employed as the base information. Research has shown that while flooding occurs in open areas (e.g., bare soil or scarcely vegetated areas), smooth water surfaces replace rough surfaces and reflect the radar signal in the specular direction at a distance from the antenna, resulting in a low backscatter and showing as dark areas in SAR images (Matgen et al., 2011; Li et al., 2019; Qiu et al., 2021). Conversely, in densely built-up areas, the above situation is commonly reversed. Due to the double scattering between the inundated road and the adjacent building walls, the post-flood backscatter is expected to be greater than before (Chini et al., 2019; Bhatt et al., 2020; Mason et al., 2021). This phenomenon leads to significant misclassification when using SAR image-based flood mapping methods (either threshold segmentation or supervised classification) (Singha et al., 2020). Similarly, the phenomenon also causes over-detection of flooded areas in the NDI-based flood mapping approach (Giustarini et al., 2013). For the difference in flood extraction caused by double bounce, previous studies have investigated the possible solution model in vegetated areas (Tsyganskaya et al., 2018; Conde and de Mata Muñoz, 2019). Nevertheless, a feasible solution for urban areas is still needed.

Introducing Land Cover Products (LCP) into urban flood mapping is potentially a feasible solution to the above-mentioned issues. In particular, for different land cover categories within LCP, different thresholds can be identified according to whether the double bounce occurs or not during the flood event, thereby increasing the accuracy of urban flood extraction. However, this could result in an increase in computational complexity. In recent years, high-performance cloud computing platforms have been developed, including Google Earth Engine (GEE). Relying on Google Cloud, GEE can deal with computationally intensive geospatial data analysis (Gorelick et al., 2017), allowing users to take advantage of LCP in urban flood mapping. This paper, therefore, presents a timely approach to urban flood mapping based on GEE by combining SAR with LCP. The key research questions addressed in this research include: 1) Which land cover types can be grouped to augment existing flood mapping approaches? 2) What flood mapping approach can be used for each category?

2 Materials and methods

2.1 Flood cases

In this research, we present two use cases to demonstrate the utility of the proposed approach.

Case 1: In August-September 2017, Hurricane Harvey hit Texas, USA (Figure 1A). On 25 August 2017, Harvey struck the

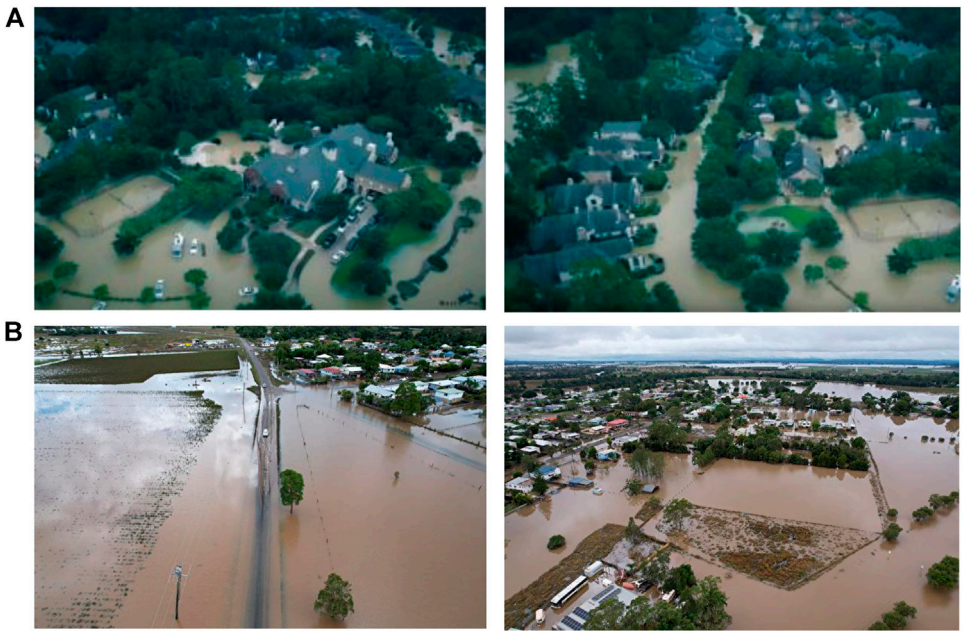

FIGURE 1
Oblique aerial photographs taken over **(A)** flooded urban areas in the Barrington Kingwood area, Houston (Chini et al., 2019); **(B)** flooded roads and houses in Coraki, Australia, 7 March 2022 (Photo by Dan Peled/Getty Images).

Texas coast and caused 1317.75 mm of rain at Cedar Bayou (NASA earth observatory, 2022). Thereafter, Harvey continued to move towards the Northwest, staying in Texas for over 60 h (National Oceanic and Atmospheric Administration, 2022). Harvey produced 24 trillion gallons of cumulative rainfall, more than any other storm in the U.S. meteorological record, causing $125 billion in economic damage (United States National Hurricane Center, 2022). This disaster severely affected Houston, impacting it with the same amount of rainfall as usually falls in an entire year. From 26 August to 30, flooding occurred in various areas throughout the entire city, as evidenced in aerial photography (Figure 1A).

Case 2: In late February to early March 2022, 2 weeks of continuous rainfall in Australia caused flooding that killed 22 people and inundated thousands of homes in Queensland and New South Wales (Center for Disaster Philanthropy, 2022). On 7 March, the flood appeared in Coraki, Australia, hitting roads and houses. Figure 1B shows photos taken in flood affected urban areas in Coraki from 7 to 9 March 2022.

2.2 Data collection

2.2.1 SAR images

The SAR images used in this paper are Sentinel-1 SAR ground range detected (GRD) products, which are available as GEE built-in datasets and ready to import for direct use. This paper selected the Interferometric Wide (IW) swath acquisition mode and VV polarised SAR images. IW mode is the main acquisition mode over land and is used primarily for land feature acquisition. For the choice of polarisation method, VH is generally used for flood extraction in open areas due to its strong sensitivity to smooth water surface. However, urban areas present significant vertical undulations caused by infrastructure such as buildings. In this scenario, VV polarisation, which is sensitive to vertical structures, could achieve higher accuracy. Combining VV and VH (e.g. ratio) is a practical approach in vegetation related research, while tends to be less sensitive compared with VV in urban settings. In addition, VV polarisation enables clear identification of inundation features and provides satisfactory results for mapping inundated areas (Conde and de Mata Muñoz, 2019). Therefore, VV polarisation is adopted to simplify the process and to realise rapid urban flood mapping. For the two flood use cases, we selected one flooded SAR image and five non-flooded SAR images as reference images for analysis (Table1).

2.2.2 Land use mapping products

Two LCPs were used in this paper. The National Land Cover Database (NLCD) 2016 was used for the Houston flood case. The NLCD is a set of products developed by the U.S. Geological Survey (USGS) in collaboration with several federal agencies, and has been released in five versions over the past 2 decades: NLCD 1992, 2001, 2006, 2011 and 2016. These products provide

TABLE 1 The selected Sentinel-1 satellite datasets for Houston flood and Coraki flood.

	Image acquisition Time [UTC]	Mode	Polarization	Pixel size (m)	Direction of the orbit	Flood or Reference
Houston flood	2017-08-30T12:22:32	IW	VV	10	Descending	Flood
	2017-08-06T12:22:05	IW	VV	10	Descending	References
	2017-08-12T12:22:47	IW	VV	10	Descending	References
	2017-08-18T12:22:05	IW	VV	10	Descending	References
	2017-09-23T12:22:07	IW	VV	10	Descending	References
	2017-09-29T12:23:19	IW	VV	10	Descending	References
Coraki flood	2022-03-07T19:14:20	IW	VV	10	Descending	Flood
	2022-01-06T19:14:21	IW	VV	10	Descending	References
	2022-01-30T19:14:20	IW	VV	10	Descending	References
	2022-02-11T19:14:20	IW	VV	10	Descending	References
	2022-02-23T19:14:20	IW	VV	10	Descending	References
	2022-03-07T19:14:20	IW	VV	10	Descending	References

spatially reliable information on the country's land cover. Compared to previous products, NLCD 2016 achieved an overall accuracy of up to 86.4% and 90.6% for Overall Level II and I, respectively (Wickham et al., 2021). At the same time, the NLCD 2016 product is the closest to the time of the Houston floods (2017) and, therefore, provides the most appropriate land cover information for the Houston flood (Multi Resolution Land Characteristics Consortium, 2022). Based on NLCD EVA (Enhanced Visualization and Analysis) tool, the changing area percentage in Houston from 2016 to 2019 is 3.02% (NOAA's Office for Coastal Management, 2022). Such a small rate will not influence the analytical results and the uncertainty is within the acceptable range of this study.

The Coraki flood analysis used New South Wales (NSW) 2017 Landuse mapping. This product classifies land use using the aerial and satellite sensor imagery available for NSW over the past 5-to-10 years, including, but not limited to; digital aerial imagery (ADS) captured by the NSW Department of Customer Service (DCS), fine spatial resolution urban ADS captured on behalf of DCS, SPOT 5, 6 and 7 (Airbus), Planet™, Sentinel 2 (European Space Agency) and LANDSAT (NASA) satellite sensor imagery. The 2017 Landuse dataset identifies how the NSW landscape has been used for food production, forestry, nature conservation, infrastructure and urban development at the scale of 1:10,000 (The Central Resource for Sharing and Enabling Environmental Data in NSW, 2022).

2.2.3 Auxiliary data

We used the flood raster from the Maxar Open Data Program and optical images from the GEE built-in Sentinel-2 dataset as validation datasets for the Houston and Coraki floods, respectively. The raster image provided by the Maxar open data program was acquired on 30 August 2017, the same time as the SAR image. Sentinel-2 optical images were acquired on 21 March 2022, with no flooding on the land surface, but significant flood marks, which can be used to determine the extent of flooding.

For refining purposes, the JRC Global Surface Water Dataset and WWF HydroSHEDS digital elevation model were incorporated to remove pixels that were misclassified as flood from fixed water bodies and on slopes >5. The JRC Global Surface Water dataset contains maps of the location and temporal distribution of surface water from 1984 to 2020, and provides statistical information on the extent and variability of these water surfaces. It was proposed in 2016 and it used three million Landsat satellite sensor images to capture surface water bodies from 1984 to 2015 at 30 m spatial resolution. HydroSHEDS was a hydrologically conditioned elevation dataset developed by the Conservation Science Program of the World Wildlife Fund. It is based primarily on elevation data obtained during NASA's Shuttle Radar Topography Mission (SRTM) (Pekel et al., 2016).

2.3 Method

A system flow diagram representing the processing methodology is shown in Figure 2. The proposed method consists of three major processes. 1) Pre-processing: clipping the study area and using different functions to calculate the NDI for each partitioned area. 2) Flood extraction: mapping flood area using threshold segmentation. 3) Post-processing: stitching each single flood map together and refining morphologically.

2.3.1 Study area segmentation

In this paper, the study area was segmented based on the land cover types in the LCP. The classification was designed based on whether a double-bounce is expected to occur or not. We

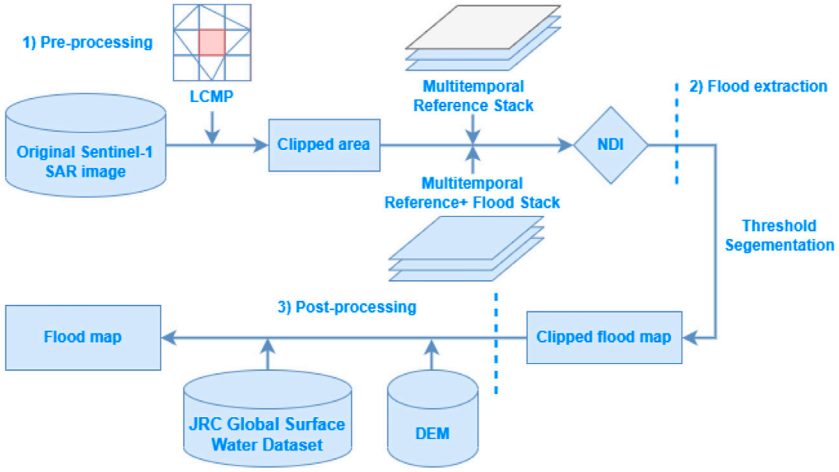

FIGURE 2
System flow diagram describing the methodology for combining LCP and SAR data to map urban flooding.

TABLE 2 Optical and SAR sub-images of each class.

	Built-up		Vegetation		Open areas	
	High intensity developed	Low intensity developed	Tall vegetation	Shrub	Barren	Wetland
Houston	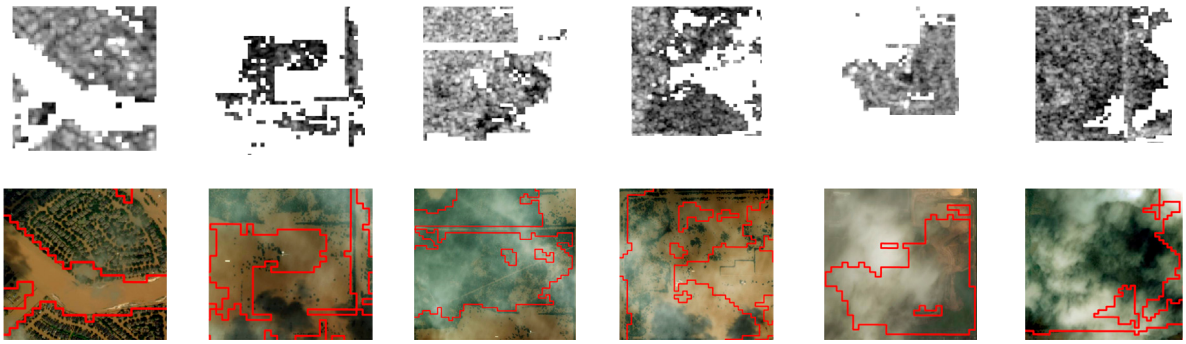					
Coraki	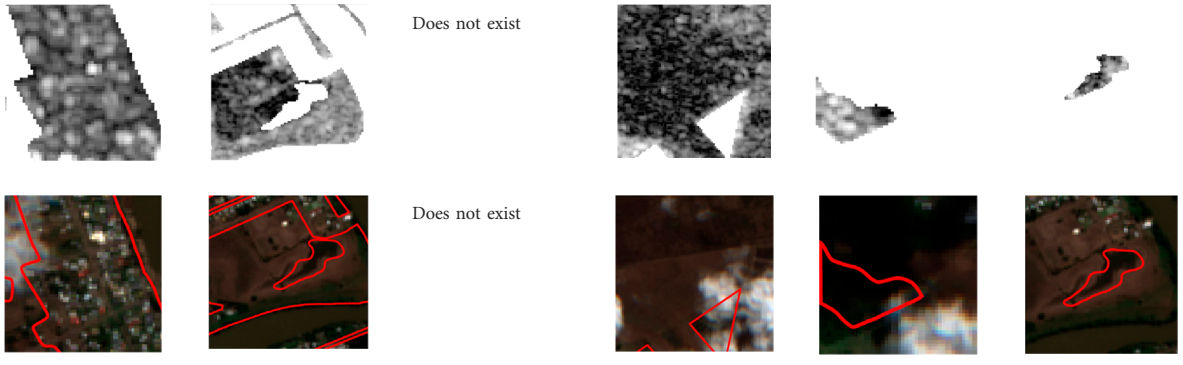		Does not exist			
			Does not exist			

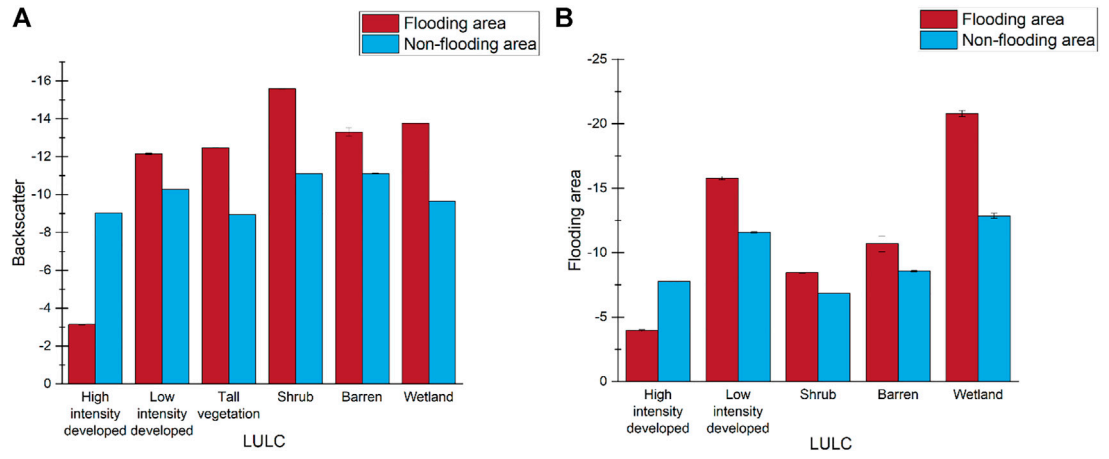

FIGURE 3
Average backscatter in flooding *versus* non-flooding areas for **(A)** Houston and **(B)** Coraki.

classified the land use types initially into three main categories according to the LCP: built-up, vegetation and open areas, each subdivided into two sub-categories. Built-up includes high intensity developed and low intensity developed. High intensity developed represents areas with building density over 50%, including commercial and residential areas and service buildings. Low intensity developed areas with less than 50% building density involve roads, goods storage, parks and recreational facilities (e.g. stadiums, golf courses). Vegetation includes shrub and tall vegetation. Shrub includes mainly grassland, scrub, fields and pasture. Tall vegetation refers mainly to trees and woodland. Open areas include Barren and Wetland. Within each land cover classification or segmentation, light or dark spots were identified in the flooded areas in the SAR images, as illustrated in Table 2.

Table 2 shows that the flooded areas in low intensity developed, tall vegetation, shrub, barren, and wetland are all dark spots, demonstrating that these land use-land cover (LULC) types do not double-bounce during flooding. On the contrary, high intensity developed land has bright flooded areas, indicating a double-bounce. To demonstrate the double bounce effects, we further acquire the backscatter of the flooded areas and non-flooded areas for different LULC types, as shown in Figure 3. Clearly, the backscatters of flooding areas are higher than non-flooding areas in the high intensity developed land. Conversely, the backscatter of flooding areas for all other LULC types is lower than the non-flooding areas. Based on these observations, the study area was divided into two categories: Non-Double-Bounce Areas (NDBA, including low intensity developed, tall vegetation, shrub, barren, and wetland) and Double-Bounce Areas (DBA, including high intensity developed).

2.3.2 Normalised difference index

We used multi-temporal statistics of SAR images to calculate the normalised difference index (NDI) as proposed by Cian et al. (2018). The method constructs stacks with reference images only and reference images-plus-flooded images, and derives the NDI from these two image stacks. The method was tested in the 2010 Veneto (Italy) flood and 2015 floods in Malawi and Uganda and demonstrated reliable and effective accuracy in extracting flood areas.

Here, we employed two different methods to calculate the NDI for two types of partitioned areas. In the NDBA, the backscatter of the flooded area reduces. For this reason, the minimum pixel value of the stacks with (flood, reference) images and the mean pixel value of the reference stack were used to calculate the NDI_{fn} as:

$$NDI_{fn} = \frac{min(flood, reference) - mean(reference)}{min(flood, reference) + mean(reference)}$$

Where the units of the input data are the linear scale. Since the decibel is linked to the total intensity directly, a linear scale can be derived from the decibel representing the total intensity (Schmitt et al., 2015).

In the DBA, the backscatter increases while those areas experience flooding. In this paper, the NDI_{fd} was derived by the maximum pixel value of the (flood, reference) stacks and the mean pixel value of the reference stack as:

$$NDI_{fd} = \frac{max(flood, reference) - mean(reference)}{max(flood, reference) + mean(reference)}$$

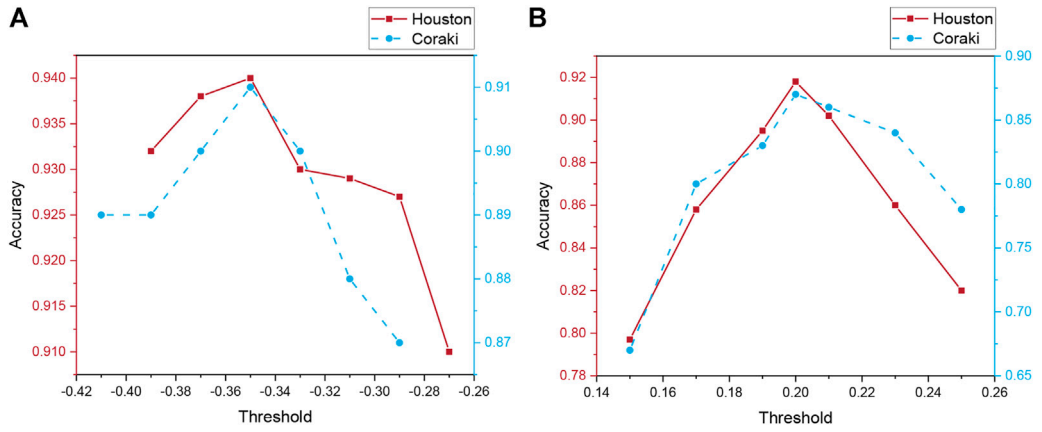

FIGURE 4
Segmentation accuracy at DBA and NDBA in the Houston and Coraki: **(A)** flood segmentation accuracy at different segmentation thresholds for DBA; **(B)** NDBA flood segmentation accuracy at different segmentation thresholds.

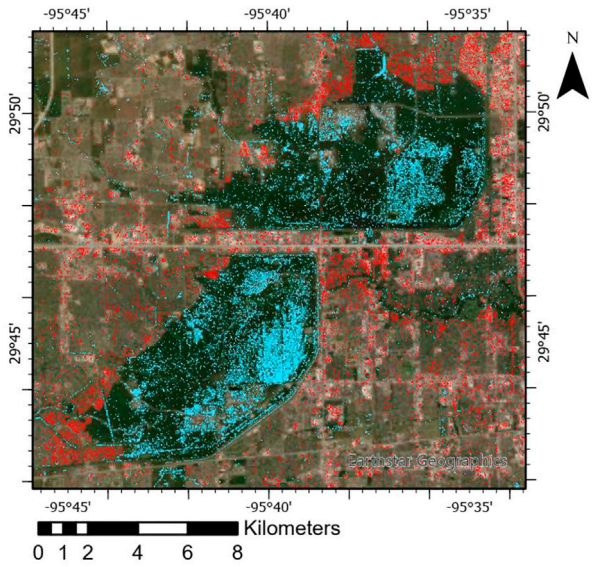

FIGURE 5
Flood map of Houston: red for flooding in DBA, blue for flooding in NDBA.

2.3.3 Thresholding

After computing the NDI_{fn} and NDI_{fd}, it is necessary to acquire the appropriate thresholds to extract the flooded areas in both cases. The common method to obtain thresholds includes empirical based and automatic approach. For empirical approach, no single threshold is applicable on a global scale. For automatic thresholding, it performs generally well in large basin floods (Martinis et al., 2009). However, in urban areas, the accuracy of the thresholds is low since the flooded water bodies are not significantly different from other features, and the statistical histograms do not show an apparent bimodal distribution. Therefore, based on previous research, we emulated the parameter tuning process in machine learning to obtain the threshold (Liang and Liu, 2020). With an iteration step of 0.02, we limited the DBA threshold range from -0.42 to -0.26 and the NDBA threshold range from 0.14 to 0.26. Within these ranges, we iterate in steps of 0.02 to assess accuracy. The classification accuracies under different thresholds are shown in Figure 4, with the highest accuracies highlighted. For both study areas, the appropriate DBA flood segmentation threshold was -0.35 and the appropriate NDBA flood segmentation threshold was 0.2 (Figure 4). Therefore, these two thresholds were selected as segmentation thresholds in this paper.

2.3.4 Post-processing

The extracted urban flooding area can be affected by external factors and, thus, a post-processing refinement is necessary. The refinement was carried out in three ways: 1) Removing fixed water bodies. The JRC Global Surface Water dataset was used to remove stable water bodies that have been present for over 10 months 2) Excluding areas of high slope. In this research, the WWF HydroSHEDS digital elevation model was used to remove pixels from areas where the surface slope exceeded 5%. 3) Trimming edge areas. Flooded edges in urban flooded areas are often misclassified due to SAR image resolution and extraction accuracy issues, with non-flooded area pixels being identified as flooded areas. Thus, we removed all pixels with less than nine neighbouring flooded pixels.

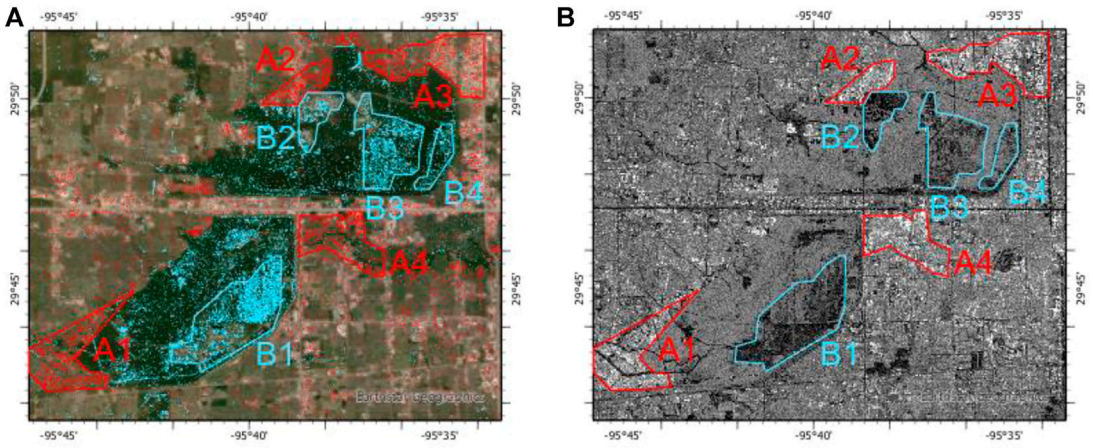

FIGURE 6
Extracted flooded areas from **(A)** optical and **(B)** SAR images in the Houston flood case. A1 Cinco Ranch Southpark, A2 Bear Creek Central, A3 Heritage Business Park, A4 Energy Corridor; B1 George Bush Park, B2 Addicks/Park Ten (West), B3 Addicks/Park Ten (Middle), B3 Addicks/Park Ten (East).

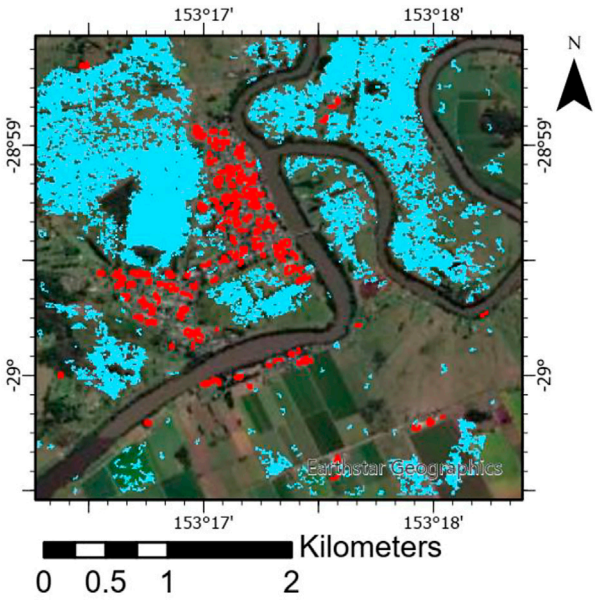

FIGURE 7
Flood map of Coraki: red for flooding in DBA, blue for flooding in NDBA.

3 Results

3.1 Houston, texas

Figure 5 shows the Houston flood mapping results, with the red and blue areas representing flooding in the DBA and NDBA, respectively. Based on validation dataset, the classification achieved an accuracy of 92.7%.

By comparing the flood mapping in this paper with previous studies such as DeVries et al. (2020), we found that our extraction method correctly extracted the main floodplains in the Houston flood case and further highlighted the flooded roads with high accuracy (Figure 6).

3.2 Coraki, New South Wales

The flood mapping results for Coraki are shown in Figure 7, where the red areas represent floods in the DBA, and the blue areas represent floods in the NDBA. The northern areas of Coraki that were severely affected by this flood were correctly extracted, with a classification accuracy of up to 89%.

3.3 Accuracy comparison

We produced flood maps without LCP as the benchmark to test the effectiveness of our approach. Figure 8 shows the benchmark flood maps for Houston and Coraki, respectively, where poor sensitivity of flood was identified in urban areas without LCP, leading to incorrect extraction of flooding areas between buildings (Figure 8). To further compare the flood mapping methods with and without LCP, the accuracy and computational time were listed in Table 3. The LCP based flood mapping method has increased accuracy by 12.9%–17.8% compared to non-LCP based method. LCP based method has also achieved an increased computational efficiency, with average time reduction of 2s–4s (Table 3).

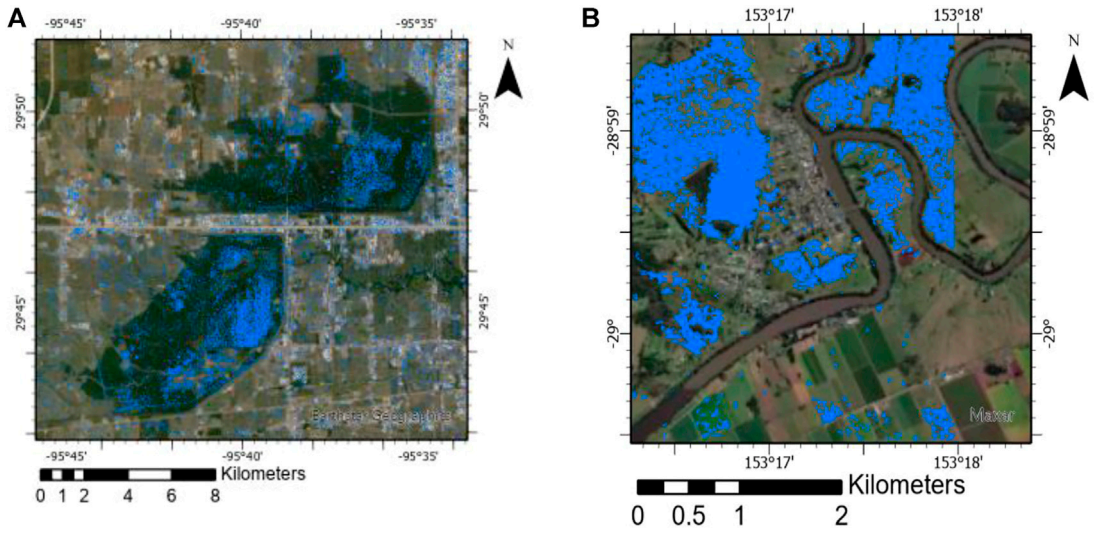

FIGURE 8
Benchmark flood maps of **(A)** Houston and **(B)** Coraki.

TABLE 3 Comparison of accuracy and computational efficiency of LCP based flood mapping method *versus* non-LCP based method.

	Houston				Coraki			
	LCP based method			Non-LCP based method	LCP based method			Non-LCP based method
	DBA	NDBA	Total (%)		DBA	NDBA	Total (%)	
Accuracy	94.0%	91.8%	92.7	76.2%	91.0%	87.0%	89.0%	74.1%
Time		48s		52s		21s		23s

4 Discussion

4.1 Study area segmentation

This paper introduces the LCP for area segmentation as an aid to the classification of flooded areas from SAR images. Compared to previous studies, the basis of the segmentation was determined by whether buildings, vegetation or barren land covers a pixel, and further subdivides all LULC types into six categories: high intensity developed, low intensity developed, tall vegetation, shrub, barren and wetland. Based on these six categories, it was possible to re-categorise them based on whether a double bounce backscatter occurs or not. Since flooding areas where double bounce occurs are bright spots in SAR images, and flooding areas where double bounce does not occur are shown as dark spots, they can be visually distinguished by cross-comparing SAR images. By making this distinction, all LULC types were combined into two categories, NDBA and DBA, accordingly. The segmentation method proposed in this paper considers practical aspects such as building density and the height of the overlying vegetation, rather than just the planned type of land, so the segmentation results are more suitable for further flood mapping. However, some issues remain when using the LCP as a data source for segmentation. For example, the administrative division used by the LCP in calculating building densities can result in some small areas with dense buildings within areas classified as low-intensity. Further research could combine the production of LCPs with flood mapping, where the production of LCPs focuses on the density of buildings around each pixel and distinguishes the type of vegetation covered on the ground using optical satellite sensor imagery. In addition to the current data source, the high-resolution LiDAR DEM could be used to differentiate urban surface conditions. LiDAR DEM data containing building surface information could help the extraction of buildings as individual objects, which allows

LCPs to achieve higher sensitivity in relation to building density. The use of LCPs generated in this way could be a feasible solution to these problems.

4.2 NDI and threshold acquisition

The proposed method in this paper has two virtual nodes in the flood extraction segment: NDI calculation and threshold segmentation. We used different NDI calculation methods for DBA and NDBA, respectively, based on the previous segmentation results. For DBA, the backscatter increases during flooding and shows as bright spots in the SAR image, such that the maximum value of (flood, reference) stack and the mean value of reference was employed to calculate the NDI. For NDBA, no double-bounce occurs during flooding, the backscatter decreases and appears as a dark spot in the SAR image. Thereby, the minimum of the (flood, reference) stack and the reference mean stack were used to calculate the NDI. The proposed NDI calculation method proposed can adapt to complex and heterogeneous urban environments. However, due to the inherent shortcomings of CD, the NDI cannot show flooded areas between buildings and under trees in forests accurately. Future research can include machine learning methods to complement the NDI calculation results by determining the value of the raster around buildings or tall plants.

By testing the effect of different thresholds, the most suitable extraction thresholds for NDBA and DBA were obtained, which were found to be 0.2 and -0.35, respectively. The flooding extraction using these two thresholds achieved an accuracy of 92.7% in Houston and 89% in Coraki, with at least 13% increase in accuracy compared to non-LCP based extraction method. The mapping accuracy of Coraki flood is lower than the Houston flood, which might be resulting from the size of Coraki study area (equivalent to only 0.06 of the Houston study area). The small size of the study area results in large fluctuations in the data, which could affect the final flood mapping results. For each study area, only two thresholds based on the NDBA and DBA were selected for flood mapping. This method simplifies the operation while maintaining high classification accuracy. In future, flood extraction thresholds could be learnt automatically for all land cover categories using decision tree based methods, to further boost accuracy.

5 Conclusion

Remote sensing using SAR is a vital tool for emergency flood event management. Currently, operational services focus on flood mapping in rural areas, as mapping in urban areas is hampered by complex backscattering mechanisms. A new method of flood mapping was proposed here through the incorporation of the LCP. The method starts by dividing all the land use types in the LCP into six categories and determining whether double-bounce occurs in each category. Multi-temporal SAR image stacks were created for the six categories based on the CD principle, and a different formula was used to calculate the NDI. The final test results for the Houston and Coraki flood cases showed that the accuracy of flood mapping exceeded 89% in both cases, with the Houston flood case achieved an accuracy up to 92.7%, where at least 13% accuracy increase compared to non-LCP based extraction method. The proposed flood mapping method simplified the approach in each area by dividing the study area and providing a novel fashion of dealing with the complex backscattering mechanisms on flood mapping in urban areas. Thanks to the low computational time, this approach could be applied to rapid urban flood mapping in near real time.

This research answers the two questions raised at the beginning of the article.

1) Which land cover types can be grouped to use the same flood mapping approach? When using LCP for classification, areas with building density >50% need to be classified as a category (DBA), and other land-use types can be grouped as one category (NDBA).
2) What flood mapping approach should be used for each category? For DBA, using the CD method to calculate NDI needs the maximum and average values of SAR multi-spatial images stack, and a threshold of -0.35 was used to extract the flood. For NDBA, calculating the NDI needs the minimum and average SAR multi-spatial image stack values and the flood extraction threshold selected as 0.2.

Further research could combine the production of LCPs with flood mapping. Other data sources such as the high-resolution LiDAR DEM data can be introduced to differentiate the urban surface conditions and create object-based LCPs. Moreover, Machine learning methods such as random forests and deep neural networks can be used to identify flood extraction thresholds and further boost accuracy.

Data availability statement

The original contributions presented in the study are included in the article/supplementary material further inquiries can be directed to the corresponding author.

Author contributions

ZW: Data curation, Formal analysis, Investigation, Methodology, Software, Visualisation, Writing—original draft, Writing—review and editing. CZ: Conceptualisation, Formal analysis, Investigation, Methodology, Visualisation, Writing—original draft, Writing—review and editing, Supervision, Project Administration PA: Methodology, Writing—review and editing, Supervision.

Funding

This work was supported by the Natural Environment Research Council [grant number NE/T004002/1]. The Lancaster University library provided open access publication fees by block grant from the RCUK for the United Kingdom Research Council funded paper.

Conflict of interest

The authors declare that the research was conducted in the absence of any commercial or financial relationships that could be construed as a potential conflict of interest.

Publisher's note

References

Bhatt, C. M., Rao, G. S., and Jangam, S. (2020). Detection of urban flood inundation using RISAT-1 SAR images: A case study of srinagar, Jammu and Kashmir (north India) floods of september 2014. *Model. Earth Syst. Environ.* 6 (1), 429–438. doi:10.1007/s40808-019-00690-z

Center for Disaster Philanthropy (2022). 2022 Australian flooding. https://disasterphilanthropy.org/disasters/2022-australian-flooding/.

Chini, M., Pelich, R., Pulvirenti, L., Pierdicca, N., Hostache, R., and Matgen, P. (2019). Sentinel-1 InSAR coherence to detect floodwater in urban areas: Houston and hurricane harvey as a test case. *Remote Sens.* 11 (2). doi:10.3390/rs11020107

Cian, F., Marconcini, M., and Ceccato, P. (2018). Normalized Difference Flood Index for rapid flood mapping: Taking advantage of EO big data. *Remote Sens. Environ.* 209, 712–730. doi:10.1016/J.RSE.2018.03.006

Cohen, S., Raney, A., Munasinghe, D., Derek Loftis, J., Molthan, A., Bell, J., et al. (2019). The Floodwater Depth Estimation Tool (FwDET v2.0) for improved remote sensing analysis of coastal flooding. *Nat. Hazards Earth Syst. Sci.* 19 (9), 2053–2065. doi:10.5194/nhess-19-2053-2019

Conde, F. C., and de Mata Muñoz, M. (2019). Flood monitoring based on the study of Sentinel-1 SAR images: The Ebro River case study. *WaterSwitzerl.* 11 (12). doi:10.3390/w11122454

Dao, D. A., Kim, D., Park, J., and Kim, T. (2020). Precipitation threshold for urban flood warning - an analysis using the satellite-based flooded area and radar-gauge composite rainfall data. *J. Hydro-Environment Res.* 32, 48–61. doi:10.1016/j.jher.2020.08.001

DeVries, B., Huang, C., Armston, J., Huang, W., Jones, J. W., and Lang, M. W. (2020). Rapid and robust monitoring of flood events using Sentinel-1 and Landsat data on the Google Earth Engine. *Remote Sens. Environ.* 240. doi:10.1016/j.rse.2020.111664

Fan, X., and Matsumoto, T. (2020). Comparative analysis on urban flood countermeasures based on life cycle thinking: A comparison between enhancing of drainage capacity project and sponge city. *Environ. - MDPI* 7 (7), 1–11. doi:10.3390/environments7070051

Giustarini, L., Hostache, R., Matgen, P., Schumann, G. J. P., Bates, P. D., and Mason, D. C. (2013). A change detection approach to flood mapping in Urban areas using TerraSAR-X. *IEEE Trans. Geoscience Remote Sens.* 51 (4), 2417–2430. doi:10.1109/TGRS.2012.2210901

Gorelick, N., Hancher, M., Dixon, M., Ilyushchenko, S., Thau, D., and Moore, R. (2017). Google earth engine: Planetary-scale geospatial analysis for everyone. *Remote Sens. Environ.* 202, 18–27. doi:10.1016/j.rse.2017.06.031

Huang, H., Chen, X., Zhu, Z., Xie, Y., Liu, L., Wang, X., et al. (2018). The changing pattern of urban flooding in Guangzhou, China. *Sci. Total Environ.* 622–623, 394–401. doi:10.1016/j.scitotenv.2017.11.358

Ke, Q., Tian, X., Bricker, J., Tian, Z., Guan, G., Cai, H., et al. (2020). Urban pluvial flooding prediction by machine learning approaches – A case study of shenzhen city, China. *Adv. Water Resour.* 145. doi:10.1016/j.advwatres.2020.103719

Li, N., and Niu, S. (2020). High-precision water segmentation from Synthetic Aperture Radar images based on local super-resolution restoration technology. *J. Radars* 9 (1), 174–184. doi:10.12000/JR19096

Li, Y., Martinis, S., Wieland, M., Schlaffer, S., and Natsuaki, R. (2019). Urban flood mapping using SAR intensity and interferometric coherence via Bayesian network fusion. *Remote Sens.* 11 (19). doi:10.3390/rs11192231

Liang, J., and Liu, D. (2020). A local thresholding approach to flood water delineation using Sentinel-1 SAR imagery. *ISPRS J. Photogrammetry Remote Sens.* 159, 53–62. doi:10.1016/j.isprsjprs.2019.10.017

Long, S., Fatoyinbo, T. E., and Policelli, F. (2014). Flood extent mapping for Namibia using change detection and thresholding with SAR. *Environ. Res. Lett.* 9 (3). doi:10.1088/1748-9326/9/3/035002

Martinis, S., Twele, A., and Voigt, S. (2009). "Natural Hazards and Earth System Sciences towards operational near real-time flood detection using a split-based automatic thresholding procedure on high resolution TerraSAR-X data," in *Hazards earth syst. Sci.* www.nat-hazards-earth-syst-sci.net/9/303/2009/.

Mason, D. C., Dance, S. L., and Cloke, H. L. (2021). Floodwater detection in urban areas using Sentinel-1 and WorldDEM data. *J. Appl. Remote Sens.* 15 (03). doi:10.1117/1.jrs.15.032003

Matgen, P., Hostache, R., Schumann, G., Pfister, L., Hoffmann, L., and Savenije, H. H. G. (2011). Towards an automated SAR-based flood monitoring system: Lessons learned from two case studies. *Phys. Chem. Earth* 36 (7–8), 241–252. doi:10.1016/j.pce.2010.12.009

Multi Resolution Land Characteristics Consortium (2022). NLCD land cover (CONUS) all years. Available at https://www.mrlc.gov/data/nlcd-land-cover-conus-all-years.

NASA earth observatory (2022). NASA satellite observes flood waters across Texas. Available at https://earthobservatory.nasa.gov/images/90873/nasa-satellite-observes-flood-waters-across-texas.

National Oceanic and Atmospheric Administration (2022). Tropical cyclone point maxima. Available at https://www.wpc.ncep.noaa.gov/tropical/rain/tcmaxima.html.

NOAA's Office for Coastal Management (2022). MRLC NLCD EVA tool. Available at https://www.mrlc.gov/eva/.

Pekel, J. F., Cottam, A., Gorelick, N., and Belward, A. S. (2016). High-resolution mapping of global surface water and its long-term changes. *Nature* 540 (7633), 418–422. doi:10.1038/nature20584

Peng, B., Huang, Q., Vongkusolkit, J., Gao, S., Wright, D. B., Fang, Z. N., et al. (2021). Urban flood mapping with bitemporal multispectral imagery via a self-supervised learning framework. *IEEE J. Sel. Top. Appl. Earth Observations Remote Sens.* 14, 2001–2016. doi:10.1109/JSTARS.2020.3047677

Pervin, I. A., Rahman, S. M. M., Nepal, M., Haque, A. K. E., Karim, H., and Dhakal, G. (2020). Adapting to urban flooding: A case of two cities in South asia. *Water Policy* 22, 162–188. doi:10.2166/wp.2019.174

Pulvirenti, L., Chini, M., Pierdicca, N., and Boni, G. (2016). Use of SAR data for detecting floodwater in urban and agricultural areas: The role of the interferometric coherence. *IEEE Trans. Geoscience Remote Sens.* 54 (3), 1532–1544. doi:10.1109/TGRS.2015.2482001

Qiu, J., Cao, B., Park, E., Yang, X., Zhang, W., and Tarolli, P. (2021). Flood monitoring in rural areas of the pearl river basin (China) using sentinel-1 SAR. *Remote Sens.* 13 (7). doi:10.3390/rs13071384

Schmitt, A., Wendleder, A., and Hinz, S. (2015). The Kennaugh element framework for multi-scale, multi-polarized, multi-temporal and multi-frequency SAR image preparation. *ISPRS J. Photogrammetry Remote Sens.* 102, 122–139. doi:10.1016/j.isprsjprs.2015.01.007

Shahapure, S. S., Eldho, T. I., and Rao, E. P. (2010). Coastal urban flood simulation using FEM, GIS and remote sensing. *Water Resour. Manag.* 24 (13), 3615–3640. doi:10.1007/s11269-010-9623-y

Singha, M., Dong, J., Sarmah, S., You, N., Zhou, Y., Zhang, G., et al. (2020). Identifying floods and flood-affected paddy rice fields in Bangladesh based on Sentinel-1 imagery and Google Earth Engine. *ISPRS J. Photogrammetry Remote Sens.* 166, 278–293. doi:10.1016/j.isprsjprs.2020.06.011

Tayyab, M., Zhang, J., Hussain, M., Ullah, S., Liu, X., Khan, S. N., et al. (2021). Gis-based urban flood resilience assessment using urban flood resilience model: A case study of peshawar city, khyber pakhtunkhwa, Pakistan. *Remote Sens.* 13 (10). doi:10.3390/rs13101864

The Central Resource for Sharing and Enabling Environmental Data in NSW (2022). NSW Landuse 2017 v1.2. Available at https://datasets.seed.nsw.gov.au/dataset/nsw-landuse-2017-v1p2-f0ed.

Tsyganskaya, V., Martinis, S., Marzahn, P., and Ludwig, R. (2018). SAR-based detection of flooded vegetation–a review of characteristics and approaches. *Int. J. Remote Sens.* 39 (8), 2255–2293. doi:10.1080/01431161.2017.1420938

United States National Hurricane Center (2022). Tropical cyclones tables update. Available at https://www.nhc.noaa.gov/news/UpdatedCostliest.pdf.

Wang, J., Wah Yu, C., and Cao, S. J. (2022). "Urban development in the context of extreme flooding events," in *Indoor and built environment*. (Newbury Park, California: Sage Publications). 31 (1), 3–6. doi:10.1177/1420326X211048577

Wickham, J., Stehman, S. v., Sorenson, D. G., Gass, L., and Dewitz, J. A. (2021). Thematic accuracy assessment of the NLCD 2016 land cover for the conterminous United States. *Remote Sens. Environ.* 257. doi:10.1016/j.rse.2021.112357

Zhang, Q., Wu, Z., Zhang, H., Dalla Fontana, G., and Tarolli, P. (2020). Identifying dominant factors of waterlogging events in metropolitan coastal cities: The case study of Guangzhou, China. *J. Environ. Manag.* 271, 110951. doi:10.1016/J.JENVMAN.2020.110951

Zhou, H., Ye, H., Wei, X., Zhang, Z., Wang, F., Qi, Y., et al. (2019). Comparative study on water extraction methods based on sentinel-1/2: A case study of small water body in Sri Lanka. *J. Univ. Chin. Acad. Sci.* 36 (6), 795–802.